Mechatronics 56 (2018) 166–174

Contents lists available at ScienceDirect

Mechatronics

journal homepage: www.elsevier.com/locate/mechatronics

Rejecting fast narrow-band disturbances with slow sensor feedback for quality beam steering in selective laser sintering☆

Hui Xiao, Tianyu Jiang, Xu Chen*

Department of Mechanical Engineering, University of Connecticut, Storrs, CT 06269, USA

ARTICLE INFO

Keywords:
Disturbance rejection
Nyquist frequency
Control algorithm
Selective laser sintering

ABSTRACT

A fundamental problem arises in feedback control when the system is subject to fast disturbances but can only get slowly updated sensor feedback. The problem is particularly challenging when the disturbances have frequency components near or beyond the sensor's Nyquist sampling frequency. Such difficulties occur to selective laser sintering, an additive manufacturing process that employs galvo scanners to steer high-power laser beams and relies on non-contact, slow sensing such as visual feedback to enhance the product quality. In pursuit of addressing the fundamental challenge in quality control under slow sensor feedback, this paper introduces a multi-rate control scheme to compensate beyond-Nyquist disturbances with application to selective laser sintering. This is achieved by designing a special bandpass filter with tailored frequency response beyond the slow Nyquist frequency of the sensor, along with integrating model-based predictor that reconstructs signals from limited sensor data. Verification of the algorithm is conducted by both simulation and experimentation on a galvo scanner that directs the energy beam in the additive manufacturing process.

1. Introduction

Selective laser sintering (SLS) is a powder-bed based additive manufacturing technique that builds 3-dimensional (3D) parts by layer-wise processing of powder materials. It has attracted great research and commercial attention with its ability of fast prototyping and great flexibility of processing a wide range of materials. However, one main challenge in SLS is ensuring product quality and reproducibility [1], which demands high precision machine control that is robust to noise and disturbances. To be more specific, an illustration of SLS is sketched in Fig. 1. During the processing of each layer, a galvo scanner [2] directs a high-energy moving laser beam to form a cross-section layer of the part (Fig. 2). Each axis of the scanner head consists of a motor with an optical mirror attached to the shaft and a high-speed closed-loop servo that ensures fast and accurate scanning. After finishing processing one layer, the building surface is lowered by the thickness of a new layer, and new powders are spread on top of the built layer. The procedure is repeated until the entire 3D part is completed. The fundamental beam scanning mechanism is subject to disturbances that limit the quality of the final 3D printed part. On the one hand, a small error of mirror angle will lead to large projection error at the scanning surface due to the long focal length (i.e. the focusing distance between the scanner mirror and the scanning surface in Figs. 1 and 2). On the other hand, internal disturbances arise in the complex system consisting of multiple sub-modules (i.e., a "system of system" architecture). For example, the rotation of one scanner mirror can cause vibrations that transmit to the second mirror; periodic scanning of the energy beam creates oscillatory temperature variations that hinder uniform part quality [3]; vibrations induced from periodic movement of the powder roller or from the ground also obstruct high-speed high-precision additive manufacturing.

Recent research has considered disturbance suppression in galvo scanner systems by using angular positions of the mirrors (measured from internal sensors such as encoders) as feedback. Tested control algorithms include adaptive control based on recursive least-squares [4,5] or frequency-weighted minimum-variance control [6], extended PID control [7,8], predictive control [9], linear quadratic Gaussian control [10], and iterative learning control [11]. However, when the scanner subsystem is integrated into the overall SLS process, the aforementioned disturbances at the system scale are invisible to the scanner subsystem (except for the cross-coupling disturbances between two mirrors). Additional feedback is thus needed for a robust and accurate manufacturing process. Indeed, recent trends of imaging-based sensing focus precisely on providing such information for quality monitoring purposes [1,12–17].

If precision control of SLS can be achieved by using the additional imaging feedback, a world of new possibilities would open: machines could know the true status of the laser-material interaction in real time; challenging geometric features such as thin walls, lattices, and over-

---

☆ This paper was recommended for publication by Associate Editor Chennai Guest Editor.

* Corresponding author.

E-mail addresses: hui.xiao@uconn.edu (H. Xiao), tianyu.jiang@uconn.edu (T. Jiang), xchen@uconn.edu (X. Chen).

https://doi.org/10.1016/j.mechatronics.2018.09.002
Received 6 April 2017; Received in revised form 12 August 2018; Accepted 7 September 2018

hang can be precisely made as desired; and ultimately, registration and recovery from operation failures could happen autonomously to drastically save production cost and time. While imaging-based sensing is becoming popular for manufacturing applications, precision SLS control based on such measurement feedback remains a major challenge because data-intensive sensors (e.g., CCD and infrared cameras) refresh the data frames slowly compared to the speed of material processing. Once the mechanical motion or disturbance frequency is close to or beyond the Nyquist frequency of the slow sensors, unobserved performance loss occurs, and classic controls become incapable to guarantee a precise and reliable SLS. Such fundamental challenge of control design considering beyond-Nyquist performance occurs also to other application domains, such as vision-based servo [18], optical coherence tomography (OCT) [19,20] and confocal microscopy [21]. Although we focus on additive manufacturing in this study, we will abstract our algorithm to allow for easy adaptation to these broad application domains.

From the viewpoint of control design, reconstruction of intersampling information is key when considering beyond-Nyquist disturbance rejection. Certainly, recovering an arbitrary random signal is impossible. Celebrated results by Shannon and its extensions [22,23] attest to the fact that a continuous signal can be recovered from periodically sampled data only if it is band-limited below Nyquist frequency. Many reconstruction methods exist to approximate the original information-rich signal based on different assumptions [23]. For example, Yamamoto et al. [24] formulates the problem to a maximum error minimization problem and utilizes sampled-data H_∞ control theory to find the best approximation under the H_∞ norm. Assuming a fast system model is given and the integrative sensor dynamics are available, Tani et al. [25] estimates intersample state of motion from slow and blurred images. Most literature focuses on signal reconstruction under a feedforward design scheme. In a feedback closed-loop scenario, however, a greater challenge arises, as approximation errors may be amplified after going through the closed-loop dynamics, and major feedforward techniques are not applicable here. This paper provides a novel feedback framework that remedies these significant barriers when the beyond-Nyquist signals consist of narrow bands in frequency spectrum. Our main theoretical contribution is to provide a mixed-rate feedback control scheme for compensating beyond-Nyquist disturbance by introducing a forward-model disturbance observer and a model-based intersample data predictor. From the viewpoint of application, this paper provides a first-instance systematic study of the control problem in galvo-scanning enabled additive manufacturing systems and the like. Building on top of the scanner's baseline control loop, the forward-model disturbance observer ensures closed-loop stability and separates the slow-sampled disturbance signal from the output signal. Based on the frequency distribution of the disturbance, the proposed model-based predictor then reconstructs the disturbance signal into a fast sampled one, enabling the possibility of *exact* disturbance rejection at a higher sampling rate. The proposed algorithm builds upon our recent work [26] to address general band-limited disturbances at multiple frequency locations, and drastically expands the design freedom by leveraging an infinite-impulse-response (IIR) structure in contrast to the previous finite-impulse-response (FIR) design.

The remainder of this paper is organized as follows. Section 2 formulates the disturbance rejection problem. The proposed multi-rate servo scheme for disturbance rejection of beyond-Nyquist frequency is presented in Section 3. Section 4 discusses the design of model-based predictor that uses the disturbance structure to reconstruct fast-sampled signals. Section 5 shows simulation as well as experimental results on a dual-axis galvo scanner system, and finally, Section 6 concludes this paper. A preliminary version of the paper is presented in [27]. This paper is a substantially extended study that includes the full mathematical proofs and new theoretical and experimental results.

Notations: $\mathbb{Z}^+$denotes the set of positive integers. $P_c(s)$ and $P_d(z)$ denote the continuous and discrete transfer functions of a controlled plant, respectively. $P(e^{j\omega})$ is the frequency response of $P(z)$ at frequency ω, with its real part and imaginary part denoted as $\Re P(e^{j\omega})$ and $\Im P(e^{j\omega})$. We use $\mathscr{H}$ to represents a zero order hold (ZOH) whose transfer function is $H(s) = (1 - e^{-sT_s})/s$, if the sampling period is T_s. $\lceil x \rceil$ denotes the nearest integer greater than or equal to x.

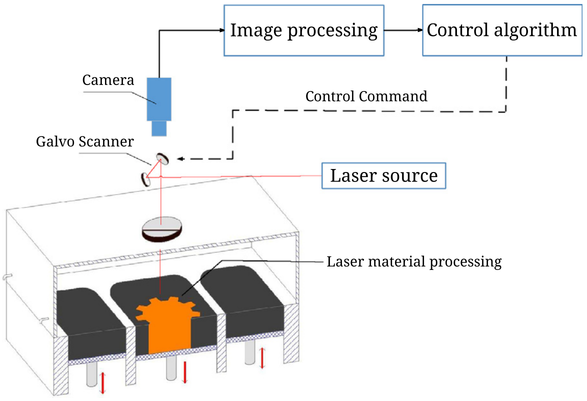

Fig. 1. Galvo scanner system in selective laser sintering process.

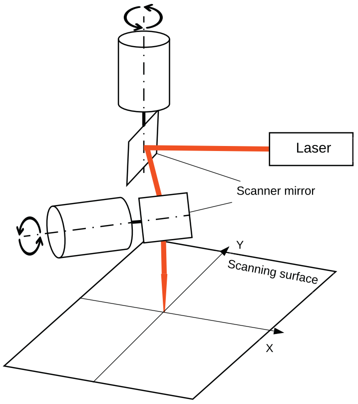

Fig. 2. Galvo scanning illustration.

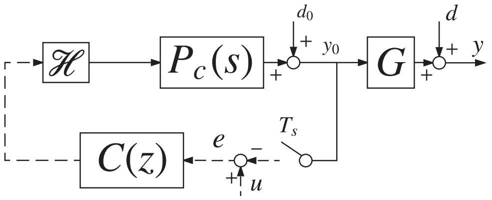

Fig. 3. Block diagram of a galvo control system.

2. Problem formulation

Recall Fig. 1. The galvo scanner is placed before an optical focusing system (e.g. an F-theta lens) so that the laser beam maintains uniform energy density as much as possible across the entire material surface. Fig. 3 shows the block diagram of the scanner control system. The main elements here include the continuous-time plant $P_c(s)$, the discrete-time controller $C(z)$, and the signal holder $\mathscr{H}$. The scanner mirror's angular position y_0 is measured by an encoder at a fast sampling rate $f_{sf} = 1/T_s$. The system output of interest to this paper is the actual position of the laser spot y. G stands for the coordinate transformation of the optical path from y_0 to y, which is defined by the optical system's forward kinematics.

For a more concise description, we classify the system disturbances into two parts. Disturbance that influences the angular position of the galvo mirror is denoted as d_0 (such as the vibration of the mirror support, or torque disturbance of the motor); disturbance d is caused by the

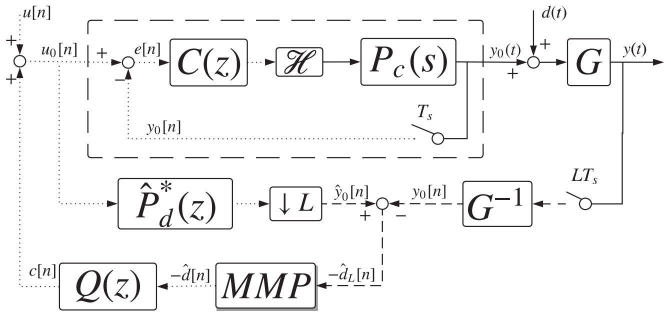

Fig. 4. Multi-rate control scheme for beyond Nyquist disturbance rejection.

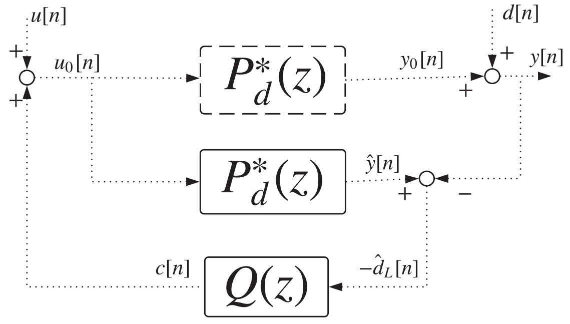

Fig. 5. Forward-model disturbance observer.

vibration of the optical system, or the atmospheric turbulence that can impact the beam path. In order to reject d_o, one can choose a high-speed encoder and design a suitable PID controller, H_∞ controller, or observer-based controller, etc. The focus of this paper is on the more challenging rejection of d, to which the internal controller does not have direct access.

Because of the highly repetitive laser scanning process [3], it is fundamentally important to understand how to address disturbances in the structure of

$$d(t) = \sum_{i=1}^{m} \lambda_i \sin(2\pi f_i t + \phi_i), \tag{1}$$

where m denotes the number of frequency components of the disturbance. Such a model encompasses the aforementioned disturbances in the first paragraph of the introduction. The frequencies f_i's are assumed known (can be derived or identified, see, e.g., [28–30]), but the amplitude λ_i's and phase ϕ_i's are unknown. In order to reject disturbance d, a slow external sensor such as a camera is used to measure the beam position y (Fig. 1). The processed data comes from the external sensor has a much slower sampling rate f_{ss}(compared to f_{sf}), that is, the measurements are incapable to capture all frequency components of the disturbance (i.e. there exist f_i such that $f_i > f_{ss}/2$). Under such a problem configuration, the goal is to design a control system to fully reject the disturbance d at a fast sampling rate of f_{sf}.

3. Multi-rate control scheme for beyond-Nyquist disturbance rejection

The proposed multi-rate control scheme is presented in Fig. 4. The sampled signals are divided into two groups, each with a different sampling rate: one group is fast sampled at f_{sf}—indicated by the dotted lines, and the other slowly sampled at $f_{ss} = f_{sf}/L$ ($L \in \mathbb{Z}^+$), as indicated by the dashed lines. Solid lines represent continuous-time signals. The block with a down arrow and L denotes a decimator that downsamples the signal by an integer factor L. The inner galvo scanner control loop is updated at a high-speed f_{sf}, and it is assumed that $f_{sf}/2 > f_{max}$, where f_{max} is the highest frequency of the system disturbances.

We refer to the structure in the dashed box in Fig. 4 as the baseline control loop, with its discrete transfer function denoted as $P^*_d(z)$. The baseline control loop can be as simple as a pre-tuned PID controller with direct negative feedback, as is shown in the figure, or some more complex feedback/feedforward control scheme. $\hat{P}^*_d(z)$ in Fig. 4 is the identified plant model of the baseline control loop. The external sensor measures $y(t)$, i.e., the position of laser beam on the scanning surface, at a slower sampling rate — L times slower than f_{sf} in this study. G^{-1} stands for the inverse coordinate transformation that is defined by the inverse kinematics of the optical system. $Q(z)$ and the multirate model-based predictor (MMP) are two key elements of the proposed servo scheme. They will be discussed in the following subsections and Section 4, respectively.

3.1. *Forward model disturbance observer*

To illustrate the design concept, we consider controlling behavior of the closed loop at a common sampling rate first. To that end, we model the galvo scanner subsystem (dashed block in Fig. 4) as $P^*_d(z)$, assume $\hat{P}^*_d(z) = P^*_d(z)$, omit the MMP block and cancel out G with G^{-1}. Then the structure of the disturbance compensation algorithm reduces to Fig. 5, a special case of the all-stabilizing Youla–Kucera parametrization [31]. The transfer function of the system output $y[n]$ (denoted as $Y(z)$) can be derived as

$$Y(z) = P^*_d(z)U(z) + (1 - P^*_d(z)Q(z))D(z). \tag{2}$$

The relationship between the command signal $u[n]$ and the system output $y[n]$ is thus independent from the feedback loop. In addition, the feedback loop introduces additional dynamics between disturbance $d[n]$ and $y[n]$. Such disturbance observer structure (as shown in Fig. 5) enables the possibility and convenience of flexible, high-performance disturbance rejection. More specifically, if we design the filter $Q(z)$ such that

$$1 - P^*_d(e^{j\omega_i})Q(e^{j\omega_i}) = 0, \tag{3}$$

where ω_i is the disturbance frequency in radians per second, then the last term of Eq. (2) will be canceled out at $z = e^{j\omega_i}$, leading to full disturbance rejection at that frequency. Moreover, the closed-loop dynamics dictate that the system remains stable if $P^*_d(z)$ is stable (automatically satisfied since it is the closed-loop transfer function of the baseline system) and if the filter $Q(z)$ is designed to be stable.

3.2. *Design of filter* Q(z)

The trivial solution to Eq. (3) (i.e. $Q(z) = P^{*-1}_d(z)$) is not always feasible because $P^{*-1}_d(z)$ may not be a proper transfer function, or have unstable poles that will challenge system stability. However, an exact full inversion of $P^{*-1}_d(z)$ is unnecessary since Eq. (3) only needs to be satisfied at ω_i. Our previous work [26] introduced a stable $Q(z)$ design that satisfies Eq. (3) at a single frequency ω_0. In addition, the design also maintains a small gain to $|1 - P^*_d(e^{j\omega})Q(e^{j\omega})|$ when $\omega \neq \omega_0$, which is important for avoiding amplifying noise and other frequency components in $d[n]$. In this subsection, we extend the point-wise stable inversion design to the case with multiple disturbance frequencies.

Theorem 1. *Let T_s be the sampling time in Fig. 5 and $\{\omega_i = 2\pi f_i T_s\}_{i=1,2,\ldots,m}$ be a set of frequencies in rad/sec at which disturbance rejection is desired. Let $P^*_d(e^{j\omega_i})$ be the frequency response of $P^*_d(z)$ at ω_i, and assume that $|P^*_d(e^{j\omega_i})| \neq 0$, $i = 1, 2, \ldots, m$.*[1] *Let $p = 2m - 1$, and*

$$Q(z) = Q_0(z)(q_0 + q_1 z^{-1} + \ldots + q_p z^{-p}), \tag{4}$$

---

[1] Otherwise the plant will not respond to input at the target frequencies. That is, input disturbance at ω_i will not impact the plant output (inherently rejected), and output disturbance at ω_i will be immune to feedback controls because the plant does not pass through any signal components at the target frequency.

with

$$\begin{bmatrix} q_0 \\ \vdots \\ q_p \end{bmatrix} = \begin{bmatrix} 1 & \cos\omega_1 & \cdots & \cos p\omega_p \\ 0 & \sin\omega_1 & \cdots & \sin p\omega_p \\ \vdots & \vdots & \ddots & \vdots \\ \vdots & \vdots & \ddots & \vdots \\ 1 & \cos\omega_p & \cdots & \cos p\omega_p \\ 0 & \sin\omega_p & \cdots & \sin p\omega_p \end{bmatrix}^{-1} \begin{bmatrix} \frac{\Re P_d^*(\mathrm{e}^{j\omega_1})}{|P_d^*(\mathrm{e}^{j\omega_1})|^2} \\ \frac{\Im P_d^*(\mathrm{e}^{j\omega_1})}{|P_d^*(\mathrm{e}^{j\omega_1})|^2} \\ \vdots \\ \vdots \\ \frac{\Re P_d^*(\mathrm{e}^{j\omega_p})}{|P_d^*(\mathrm{e}^{j\omega_p})|^2} \\ \frac{\Im P_d^*(\mathrm{e}^{j\omega_p})}{|P_d^*(\mathrm{e}^{j\omega_p})|^2} \end{bmatrix}, \tag{5}$$

$$Q_0(z) = 1 - \prod_{i=1}^{m} \left(\frac{1}{2} \frac{1 + 2k_{1,i}(1 + k_{2,i})z^{-1} + (1 + k_{2,i})z^{-2}}{1 + k_{1,i}(1 + k_{2,i})z^{-1} + k_{2,i}z^{-2}} \right), \tag{6}$$

where

$$k_{1,i} = -\cos(\omega_i), \tag{7}$$

$$k_{2,i} = \frac{1 - \tan(\pi\Omega_i T_s)}{1 + \tan(\pi\Omega_i T_s)}. \tag{8}$$

Then Eq. (3) holds for each ω_i, and the amplification at $\omega \neq \omega_i$ is controllable by choosing Ω_i, the 3-dB disturbance-rejection bandwidth of $Q_0(z)$ centered around ω_i.

Proof. For each ω_i, Eq. (3) has the solution

$$Q(\mathrm{e}^{j\omega_i}) = \frac{1}{P_d^*(\mathrm{e}^{j\omega_i})} = \frac{\overline{P_d^*(\mathrm{e}^{j\omega_i})}}{|P_d^*(\mathrm{e}^{j\omega_i})|^2}, \tag{9}$$

i.e.

$$\begin{cases} \Re Q(\mathrm{e}^{j\omega_i}) = \frac{\Re P_d^*(\mathrm{e}^{j\omega_i})}{|P_d^*(\mathrm{e}^{j\omega_i})|^2} \\ \Im Q(\mathrm{e}^{j\omega_i}) = -\frac{\Im P_d^*(\mathrm{e}^{j\omega_i})}{|P_d^*(\mathrm{e}^{j\omega_i})|^2} \end{cases}, i = 1, 2, \ldots, m. \tag{10}$$

Define first

$$Q^*(z) = q_0 + q_1 z^{-1} + q_p z^{-p} \tag{11}$$

such that $P_d^*(\mathrm{e}^{j\omega_i})Q^*(\mathrm{e}^{j\omega_i}) = 1$, then by Eq. (10), we must have, for $i = 1, 2, \ldots, m$,

$$\begin{cases} q_0 + q_1\cos\omega_i + \cdots + q_p\cos p\omega_i = \frac{\Re P_d^*(\mathrm{e}^{j\omega_i})}{|P_d^*(\mathrm{e}^{j\omega_i})|^2}, \\ q_1\sin\omega_i + \cdots + q_p\sin p\omega_i = -\frac{\Im P_d^*(\mathrm{e}^{j\omega_i})}{|P_d^*(\mathrm{e}^{j\omega_i})|^2}. \end{cases} \tag{12}$$

There are m such equation sets, or $2m$ linear equations. Since $\omega_i \in (0, \pi)$, and $\omega_i \neq \omega_j$ if $\forall i \neq j$, those linear equations are independent from each other. Then we have $2m$ linearly independent equations and $p + 1 = 2m$ unknowns, and q_i's can be uniquely solved from Eq. (5).

The first element in the Q filter in Eq. (4), or $Q_0(z)$ in Eq. (6), is a multi-band bandpass filter that has m narrow passbands centered at ω_i. It is produced by $1 - Q_1(z)$, where $Q_1(z)$ is constructed by m cascaded lattice-based band-stop filters [32,33] whose bandwidths are related to $k_{2,\,i}$'s defined by Eq. (8). One can show that $Q_0(\mathrm{e}^{j\omega_i}) = 1$ at each center frequency ω_i. Combining Eq. (6) and Eq. (11) then results in the proposed structure of $Q(z)$ in Eq. (3).

Because $Q_0(\mathrm{e}^{j\omega_i}) = 1$ and $P_d^*(\mathrm{e}^{j\omega_i})Q^*(\mathrm{e}^{j\omega_i}) = 1$, the disturbance rejection requirement (Eq. (3)) is satisfied. In addition, when $\omega \neq \omega_i$, $|Q_0(\mathrm{e}^{j\omega})|$ can be made arbitrarily small by reducing the bandwidth $B_{w,\,i}$. Thus $|1 - P_d^*(\mathrm{e}^{j\omega})Q(\mathrm{e}^{j\omega})|$ can be controlled to be approximately 1 if $\omega \neq \omega_i$, avoiding large noise amplification. □

Remark 1. If the identified model of the baseline closed-loop $\hat{P}_d^*(z)$ contains uncertainties such that $\hat{P}_d^*(z) \neq P_d^*(z)$, based on block diagram algebra, Eq. (2) becomes

$$Y(z) = \frac{P_d^*(z)U(z) + (1 - \hat{P}_d^*(z)Q(z))D(z)}{1 - Q(z)(\hat{P}_d^*(z) - P_d^*(z))}. \tag{13}$$

By using the identified mode $\hat{P}_d^*(z)$ to design $Q(z)$ based on Theorem 1, the disturbance term in Eq. (13) can still be fully rejected since Eq. (3) is satisfied. Also, by maintaining a small magnitude of Q filter at frequencies where $P_d^*(z)$ differs from $\hat{P}_d^*(z)$ (that is, by designing the magnitude of $Q(z)(\hat{P}_d^*(z) - P_d^*(z))$ in Eq. (13) to be small), the transfer function from $U(z)$ to $Y(z)$ will remain close to Eq. (2).

4. Model-based predictor design

Recall that in Fig. 4, the forward model disturbance observer works at a fast sampling rate of f_{sf}, but the sampling rate of the system output is limited to $f_{ss} = f_{sf}/L$. Consequently, a slowly sampled disturbance estimate $\hat{d}_L[n]$ is generated by the disturbance observer loop, whereas a fast sampled signal $\hat{d}[n]$ is needed to enable disturbance compensation at f_{sf}. In this section, we introduce a multirate model-based predictor to reconstruct the intersample disturbance information that is lost in the slow sampling.

Before we start discussing the model-based predictor, it is necessary to clarify some special cases where the slowly sampled disturbance is not recoverable, which are referred to as the singular frequency set σ.

Definition 1 (Singular frequency set). For disturbance that has m frequency components, a frequency distribution $f = (f_1, f_2, \ldots, f_m)$ can be considered as a point in an m-dimension space $\mathbb{R}^m$. If the slow sampling rate is f_{ss}, then the singular set consists of a group of frequency configurations defined as

$$\sigma = \left\{ f \in (\mathbb{R})^m \quad \exists f_i, f_j, \text{ s.t. } f_i = nf_{ss}/2, \text{ or } f_i \pm f_j = nf_{ss} \right\}, \tag{14}$$

where $n \in \mathbb{Z}$, $i \neq j$ and $i, j \in \{1, 2, \ldots, m\}$.

For example, let the slow sampling rate be $f_{ss} = 2$ kHz. Then a frequency distribution $f = (0.6\,\text{kHz}, 2\,\text{kHz})$ belongs to the singular frequency set because it has a frequency component (i.e $f_2 = 2$ kHz) at an integer multiple of $f_{ss}/2$. A frequency distribution $f = (0.3\,\text{kHz}, 1.7\,\text{kHz})$ also belongs to the singular frequency set because $f_1 + f_2 = f_{ss}$. In general, two scenarios contribute to a singular frequency case. The first case arises when the disturbance has one or more frequency components at the Nyquist frequency of the slow sensor (i.e., $f_{ss}/2$), or its integer multiplications. In this case, there is a DC component in the frequency domain, and the intersample signal is not recoverable without its amplitude information. The second case arises when f contains pairs of frequency components in which one frequency is the alias of the other when sampled at the slow sensor speed. Thus their time-domain signals are fused together, and amplitude information of individual components is also needed to decouple them.

If system disturbances are out of the singular frequency set (this is the more common case in practice, and the external sensor speed f_{ss} may be chosen to avoid the singularity), then based on the intrinsic signal model of $d[n]$, a fast disturbance estimate can be reconstructed by the slowly sampled $d_L[n]$ using model-based filtering, as is discussed next.

4.1. Narrow-band signal recovery with model-based predictor

Assume a multi-band signal $d_c(t)$ defined by Eq. (1) has m frequency components $f = (f_1, f_2, \cdots, f_m) \notin \sigma$ $d_L[n] = d_c(nLT_s)$ is the slow-sampled signal with sampling time LT_s, $L \in \mathbb{Z}^+$. This subsection provides the proposed approach to recover a fast-sampled signal $d[n] = d_c(nT_s)$ with sampling time T_s.

Because the fast sampling time divides the slow sampling time, every Lth sample of $d[n]$ can be obtained from $d_L[n]$ directly, i.e.

$$d[nL] = d_L[n]. \tag{15}$$

We show that the kth intersample signal ($k = 1, 2, \ldots, L - 1$) between $d[nL]$ and $d[(n + 1)L]$ (denoted as $y_k[n] \triangleq d[nL + k]$) can be recovered by

$$y_k[n] = \boldsymbol{w}_k^T \cdot \boldsymbol{\varphi}_d[n] - \boldsymbol{b}^T \cdot \boldsymbol{\varphi}_y[n]. \tag{16}$$

where $\boldsymbol{\varphi}_d[n]$ and $\boldsymbol{\varphi}_y[n]$ are data vectors defined as

$$\boldsymbol{\varphi}_d[n] \triangleq \left[d_L[n], d_L[n-1], \cdots, d_L[n-(2m-1)]\right]^T, \tag{17}$$

$$\boldsymbol{\varphi}_y[n] \triangleq \left[y_k[n-1], y_k[n-2], \cdots, y_k[n-2m]\right]^T. \tag{18}$$

$\boldsymbol{w}_k$ and $\boldsymbol{b}$ are predictor parameter vectors

$$\boldsymbol{w}_k \triangleq \left[w_{k,0}, w_{k,1}, \cdots, w_{k,(2m-1)}\right]^T, \tag{19}$$

$$\boldsymbol{b} \triangleq \left[b_1, b_2, \ldots, b_{2m}\right]^T. \tag{20}$$

The parameter vector $\boldsymbol{b}$ is composed of the coefficients of polynomial $B(z^{-1}) = 1 + b_1 z^{-1} + \ldots + b_{2m} z^{-2m}$, which is computed from expanding the product

$$B(z^{-1}) = \prod_{i=1}^{m} (1 - 2\alpha \cos(2\pi f_i L T_s) z^{-1} + \alpha^2 z^{-2}), \tag{21}$$

where $\alpha \in (0, 1)$ is a design parameter and z^{-1} is the one step delay operator.

The prediction formula (Eq. (16)) computes the kth intersample y_k by a linear combination of $2m$ consecutive samples from $d_L[n]$, as well as by a linear combination of $2m$ previous predictions about y_k. The parameters $\boldsymbol{b}$ can be calculated by Eq. (21). The algorithm of obtaining vector $\boldsymbol{w}_k$ is provided in the following theorem.

Theorem 2. *Given the above definitions, $d[n]$ can be fully recovered from $d_L[n]$ by Eqs. (15) and (16), if $f \notin \sigma$ and $\boldsymbol{w}_k$ is from the solution of*

$$\mathbf{M}_k \begin{bmatrix} h_{k,1} \\ \vdots \\ h_{k,2m(L-1)} \\ w_{k,0} \\ \vdots \\ w_{k,2m-1} \end{bmatrix} = - \begin{bmatrix} a_1 \\ a_2 \\ \vdots \\ a_{2m} \\ 0 \\ \vdots \\ 0 \end{bmatrix} + \bar{\mathbf{b}}, \tag{22}$$

$$\mathbf{M}_k \overset{\triangle}{=} [\tilde{\mathbf{M}}_k \mid \boldsymbol{e}_k \quad \boldsymbol{e}_{k+L} \quad \cdots \quad \boldsymbol{e}_{k+(2m-1)L}], \tag{23}$$

where $\boldsymbol{M}_k$ is a square matrix with a dimension of $2mL \times 2mL$; $\boldsymbol{e}_j$ is the elemental column vector whose entries are all zero except for the jth entry, which equals 1; and

$$\tilde{\boldsymbol{M}}_k \overset{\triangle}{=} \begin{bmatrix} 1 & 0 & \ldots & 0 \\ a_1 & \ddots & \ddots & \vdots \\ \vdots & \ddots & \ddots & 0 \\ a_{2m} & \ddots & \ddots & 1 \\ 0 & \ddots & \ddots & a_1 \\ \vdots & \ddots & \ddots & \vdots \\ 0 & \ldots & 0 & a_{2m} \end{bmatrix}_{2mL \times 2m(L-1).} \tag{24}$$

Parameters $\left[a_1, a_2, \ldots, a_{2m}\right]$ in Eqs. (22) and (24) come from the disturbance model $A(z^{-1}) = 1 + a_1 z^{-1} + a_2 z^{-2} + \ldots + a_{2m} z^{-2m}$, which is computed by expanding

$$A(z^{-1}) = \prod_{i=1}^{m} (1 - 2cos(2\pi f_i T_s) z^{-1} + z^{-2}). \tag{25}$$

The column vector $\bar{\mathbf{b}}$ in the rightmost of Eq. (22) contains all zeros, except for the $L, 2L, \ldots, 2mL$-th entries, which equal b_1, b_2, $\cdots$, b_{2m}.

Proof. In order to establish and validate Eq. (16), we construct a polynomial equation

$$H_k(z^{-1})A(z^{-1}) + z^{-k} W_k(z^{-L}) - B^*(z^{-L}) = 1, \tag{26}$$

where $A(z^{-1})$ is defined by Eq. (25), and

$$H_k(z^{-1}) = 1 + h_{k,1} z^{-1} + \ldots + h_{k,2m(L-1)} z^{-2m(L-1)}, \tag{27}$$

$$W_k(z^{-L}) = w_{k,0} + w_{k,1} z^{-L} + \ldots + w_{k,2m-1} z^{-(2m-1)L}, \tag{28}$$

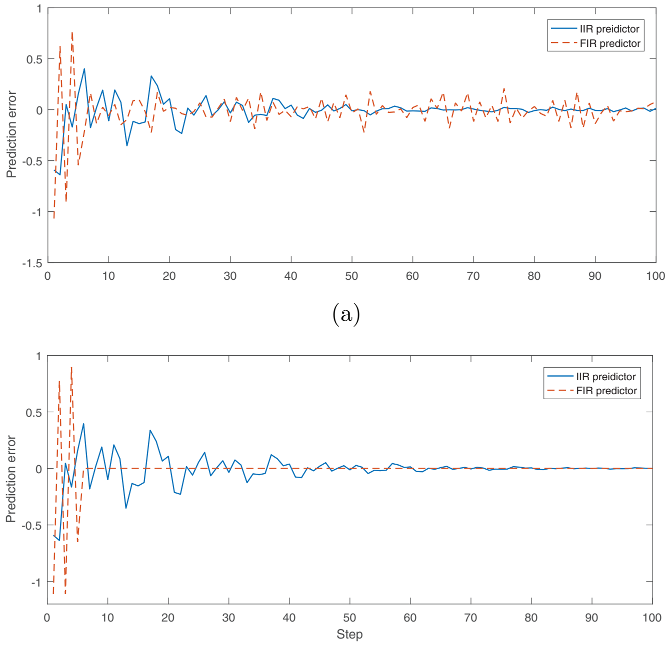

(a)

(b)

Fig. 6. Prediction error of IIR ($\alpha = 0.95$) and FIR ($\alpha = 0$) predictor, under the same configuration as Fig. 7, and the data vectors $\boldsymbol{\varphi}_d$ and $\boldsymbol{\varphi}_y$ are initialed as zero vectors. In plot (a), the input has a random noise with maximum amplitude of 0.05. The IIR predictor shows better robustness to noise. In plot (b), the input is noise-free, both the IIR and FIR predictors can make accurate predictions in steady state.

$$B^*(z^{-L}) = b_1 z^{-L} + b_2 z^{-2L} + \cdots + b_{2m} z^{-2mL}. \tag{29}$$

The coefficients of $B^*(z^{-L})$ are the same as those in $B(z^{-1})$ (computed by Eq. (21)).

Based on the internal signal model [34] of $d[n]$, $A(z^{-1})d[n] = 0$ at the steady state. Combining this with Eq. (26) yields

$$\left(1 - z^{-k} W_k(z^{-L}) + B^*(z^{-L})\right) d[n] = H_k(z^{-1}) A(z^{-1}) d[n] = 0, \tag{30}$$

which gives

$$\begin{aligned} d[n] &= z^{-k} W_k(z^{-L}) d[n] - B^*(z^{-L}) d[n] \\ &= w_{k,0} d[n-k] + w_{k,1} d[n-k-L] \cdots + w_{k,2m-1} d[n-k-(2m-1)L] \\ &\quad - b_1 d[n-L] - b_2 d[n-2L] - \cdots - b_{2m} d[n-2mL]. \end{aligned} \tag{31}$$

Replacing n with $nL + k$, we have

$$\begin{aligned} d[nL+k] &= w_{k,0} d[nL] + \cdots + w_{k,2m-1} d[(n-(2m-1))L] \\ &\quad - b_1 d[(n-1)L + k] - \cdots - b_{2m} d[(n-2m)L + k]. \end{aligned} \tag{32}$$

Recalling $d_L[n] = d[nL]$ and $y_k[n] \triangleq d[nL + k]$, it follows that Eq. (32) can be written as Eq. (16).

Now consider solving Eq. (26). Expanding the equation and collecting the coefficients of z^{-i}'s ($i = 1, 2, \ldots, 2mL$), one can get $2mL$ linear equations with $2mL$ unknowns, which can be written in matrix form as Eq. (22). □

Note that the intersample signals $y_k[n]$ are computed from not only the weighted sum of $d[n]$, but also the historical prediction values. In Eq. (21), α determines the weighting of input signals (sensor measurements) and historical prediction signals. As α gets closer to 1, the predictor will be more dependent on the historical predictions rather than input signals, thus less sensitive to the input noise (see Fig. 6a). As a trade-off, a predictor with larger α has a slower converging speed (see Fig. 6b).

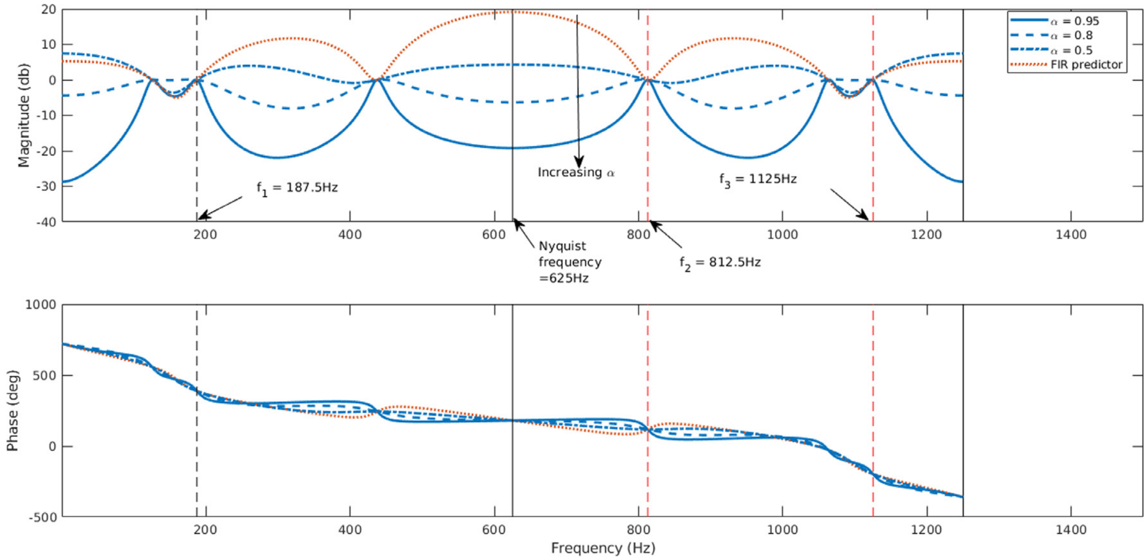

Fig. 7. Bode plot of the IIR and FIR predictor. The slow sensor sampling speed is limited to $T_s = 0.8$ ms, and $L = 3$. The disturbance has three bands at $f_1 = 187.5$ Hz, $f_2 = 812.5$ Hz and $f_3 = 1125$ Hz, two of which (red dashed lines) are beyond the Nyquist frequency ($f_N = 625$Hz).

To get more insights in choosing α, one can derive the transfer function from $d_L[n]$ to $y_k[n]$ based on Eq. (16):

$$W_k^*(z) = \frac{w_{k,0} + w_{k,1}z^{-1} + \ldots + w_{k,(2m-1)}z^{-(2m-1)}}{1 + b_1 z^{-1} + \ldots + b_{2m}z^{-2m}}, \tag{33}$$

where the denominator is computed by Eq. (21), and the numerator can be solved by Eq. (22). Fig. 7 shows the bode plot of $W_k^*(z)$ with respect to different α's. Here, the disturbances consist of three frequency components, f_1, f_2 and f_3, where f_1 is below and the other two are beyond the Nyquist frequency. As shown, a smaller α leads to a larger magnitude response. In the extreme case, if $\alpha = 0$, then the denominator of transfer function $W_k^*(z)$ becomes 1. Consequently, the predictor reduces to an FIR structure with a magnitude response above 0 dB, and the predictions are purely dependent on input signals. Therefore, an IIR predictor with a larger α is more robust to input noise; an FIR predictor is most sensitive to input noise. In practice, in order to reduce the influence of measurement noise and increase the prediction accuracy, α is recommended to be chosen closer to 1, e.g., starting with $\alpha = 0.9$. The value can be further increased when dealing with noisy applications. However, α must be less than 1, because the roots of polynomial $B(z^{-1})$ (hence the poles of $W_k^*(z)$) in Eq. (21) are at $z = \alpha e^{\pm j2\pi f_i L T_s}$ and must fall inside the unit circle to yield a stable filtering process. Note that all predictors have the same frequency response at $f = f_i, i = 1, 2, 3$, which is expected because all designs target to recover signals at those frequencies. Note also that the transfer functions have a sampling of T_s and the beyond-Nyquist frequency response is symmetric in magnitude to that below the Nyquist frequency.

4.2. Decoupled solution form and computation reduction

In Theorem 2, the dimension of $\boldsymbol{M}_k$ is scaled by the number of frequency components m and downsampling ratio L. When m and L are large, solving high-dimension linear system equations could be computationally expensive. However, it turns out that instead of solving Eq. (22), the predictor parameters can be solved from an equivalent form with reduced computation cost.

Let the augmented matrix[2] of system Eq. (22) be $\bar{\boldsymbol{M}} = [\boldsymbol{M}_k \mid \boldsymbol{b}]$, where $\boldsymbol{b}$ is the summation of vectors on the right side of Eq. (22). Observing the sparse structure of the elemental vectors $\{\boldsymbol{e}_k, \cdots, \boldsymbol{e}_{k+(2m-1)L}\}$ in $\boldsymbol{M}_k$ in Eq. (23), we can swap rows of $\bar{\boldsymbol{M}}$ to yield, without changing the solutions to the associated linear system,

$$\bar{\boldsymbol{M}} = \left[\begin{array}{cc|c} \boldsymbol{A}_{2m\times 2m(L-1)} & \boldsymbol{I}_{2m\times 2m} & \boldsymbol{b}_1 \\ \boldsymbol{B}_{2m(L-1)\times 2m(L-1)} & \boldsymbol{0}_{2m(L-1)\times 2m} & \boldsymbol{b}_2 \end{array}\right], \tag{34}$$

where $\boldsymbol{I}$ is an identity matrix, $\boldsymbol{0}$ is a zero matrix, $\boldsymbol{b}_1$ and $\boldsymbol{b}_2$ are column vectors with length $2m$ and length $2m(L-1)$. Let $\boldsymbol{h}_k = [h_{k,1} \quad \ldots \quad h_{k,2m(L-1)}]^T$, $\boldsymbol{w}_k = [w_{k,0} \quad \ldots \quad w_{k,2m-1}]^T$, then an equivalent form of Eq. (22) is

$$\begin{bmatrix} \boldsymbol{A} & \boldsymbol{I} \\ \boldsymbol{B} & \boldsymbol{0} \end{bmatrix} \begin{bmatrix} \boldsymbol{h}_k \\ \boldsymbol{w}_k \end{bmatrix} = \begin{bmatrix} \boldsymbol{b}_1 \\ \boldsymbol{b}_2 \end{bmatrix}, \tag{35}$$

or,

$$\boldsymbol{B}\boldsymbol{h}_k = \boldsymbol{b}_2, \tag{36}$$

$$\boldsymbol{w}_k = -\boldsymbol{A}\boldsymbol{h}_k + \boldsymbol{b}_1. \tag{37}$$

This suggests that one can solve system Eq. (36) first, then the predictor parameters $\boldsymbol{w}_k$ can be computed by a direct matrix-vector multiplication and a vector addition in Eq. (37).

For a better understanding of procedures of designing the IIR predictor, we give an illustrative example below.

Example 1. Consider the case where the disturbance contains one frequency component (i.e. $m = 1$) at $f = 1.2$ kHz, and the position sensor of the galvo scanner has a fast sampling rate $f_{sf} = 3$ kHz. Without loss of generality, let the external sensor's sampling rate be $f_{smax} = 1.2$ kHz, which is not fast enough because the disturbance occurs beyond the Nyquist frequency $f_N = f_{smax}/2 = 0.6$ kHz. For vision cameras, the achievable frame update rate depends on the size of field of view, and f_{smax} is reached by using the minimum view window. The proposed procedure for designing the predictor is as follows:

Choose L. This relates to f_{ss}, the sampling rate of the slow sensor, by the relationship $L = f_{sf}/f_{ss}$. Also, f_{ss} must be smaller than f_{smax}. The minimum L is then given by $L_{min} = \lceil f_{sf}/f_{smax} \rceil = 3$. Here, we choose $L = L_{min} = 3$ as an example.

Define predictor structure. The predictor is defined as (cf. Section 4.1)

$$d[3n] = d_L[n], \tag{38}$$

$$d[3n+1] = w_{1,0}d_L[n] + w_{1,1}d_L[n-1] - b_1 y_1[n-1] - b_2 y_1[n-2], \tag{39}$$

---

[2] Given a linear system equation $\mathbf{Ax} = \mathbf{b}$, the augmented matrix is defined as $\bar{\boldsymbol{A}} = [\boldsymbol{A} \mid \boldsymbol{b}]$.

$$d[3n+2] = w_{2,0}d_L[n] + w_{2,1}d_L[n-1] - b_1 y_2[n-1] - b_2 y_2[n-2]. \tag{40}$$

where $y_1[n] = d[3n+1]$ and $y_2[n] = d[3n+2]$.

Compute parameters. Use Eq. (25) and Eq. (21) to obtain a_i's and b_i's: $a_1 = -2\cos(2\pi f T_s)$, $a_2 = 1$, $b_1 = -2\alpha\cos(6\pi f T_s)$, $b_2 = \alpha^2$.

Obtain $[w_{1,0}, w_{1,1}]$. From Eqs. (22)–(24), construct

$$\begin{bmatrix} 1 & 0 & 0 & 0 & 1 & 0 \\ a_1 & 1 & 0 & 0 & 0 & 0 \\ a_2 & a_1 & 1 & 0 & 0 & 0 \\ 0 & a_2 & a_1 & 1 & 0 & 1 \\ 0 & 0 & a_2 & a_1 & 0 & 0 \\ 0 & 0 & 0 & a_2 & 0 & 0 \end{bmatrix} \begin{bmatrix} h_{1,1} \\ h_{1,2} \\ h_{1,3} \\ h_{1,4} \\ w_{1,0} \\ w_{1,1} \end{bmatrix} = \begin{bmatrix} a_1 \\ a_2 \\ b_1 \\ 0 \\ 0 \\ b_2 \end{bmatrix}. \tag{41}$$

Parameters $w_{1,0}$ and $w_{1,1}$ come from the unique solution of Eq. (41). Reorganizing the rows of corresponding augmented matrix yields

$$\tilde{\mathbf{M}} = \left[\begin{array}{cccc|cc|c} 1 & 0 & 0 & 0 & 1 & 0 & a_1 \\ 0 & a_2 & a_1 & 1 & 0 & 1 & 0 \\ a_1 & 1 & 0 & 0 & 0 & 0 & a_2 \\ a_2 & a_1 & 1 & 0 & 0 & 0 & b_1 \\ 0 & 0 & a_2 & a_1 & 0 & 0 & 0 \\ 0 & 0 & 0 & a_2 & 0 & 0 & b_2 \end{array}\right]. \tag{42}$$

Then $w_{1,0}$, $w_{1,1}$ are given by

$$\begin{bmatrix} w_{1,0} \\ w_{1,1} \end{bmatrix} = -\begin{bmatrix} 1 & 0 & 0 & 0 \\ 0 & a_2 & a_1 & 1 \end{bmatrix} \begin{bmatrix} h_{1,1} \\ h_{1,2} \\ h_{1,3} \\ h_{1,4} \end{bmatrix} + \begin{bmatrix} a_1 \\ 0 \end{bmatrix}, \tag{43}$$

where

$$\begin{bmatrix} h_{1,1} \\ h_{1,2} \\ h_{1,3} \\ h_{1,4} \end{bmatrix} = \begin{bmatrix} a_1 & 1 & 0 & 0 \\ a_2 & a_1 & 1 & 0 \\ 0 & 0 & a_2 & a_1 \\ 0 & 0 & 0 & a_2 \end{bmatrix}^{-1} \begin{bmatrix} a_2 \\ b_1 \\ 0 \\ b_2 \end{bmatrix}. \tag{44}$$

Obtain $[w_{2,0}, w_{2,1}]$. Following the same procedure as the last step, we have

$$\begin{bmatrix} w_{2,0} \\ w_{2,1} \end{bmatrix} = -\begin{bmatrix} a_1 & 1 & 0 & 0 \\ 0 & 0 & a_2 & a_1 \end{bmatrix} \begin{bmatrix} h_{2,1} \\ h_{2,2} \\ h_{2,3} \\ h_{2,4} \end{bmatrix} + \begin{bmatrix} a_2 \\ 0 \end{bmatrix}, \tag{45}$$

where

$$\begin{bmatrix} h_{2,1} \\ h_{2,2} \\ h_{2,3} \\ h_{2,4} \end{bmatrix} = \begin{bmatrix} 1 & 0 & 0 & 0 \\ a_2 & a_1 & 1 & 0 \\ 0 & a_2 & a_1 & 1 \\ 0 & 0 & 0 & a_2 \end{bmatrix}^{-1} \begin{bmatrix} a_1 \\ b_1 \\ 0 \\ b_2 \end{bmatrix}. \tag{46}$$

5. Simulation and experiment results

In this section, we present the simulation and experiment results of beyond-Nyquist disturbance compensation on a galvo scanner testbed. The dual-axis 6215H galvo scanner from Cambridge Technology Inc is used. Each axis has ±20° of scan angles and 8 μrad of repeatability. It also comes with a driver board that has a built-in motor driver circuit and pre-tuned PID-type control algorithms. The baseline closed-loop model $P_d^*(z)$ is obtained by system identification techniques [35] at a fast sampling rate of 10 kHz, and the result is

$$\hat{P}_d{}^*(z) = \frac{0.551z^{-1} + 0.356z^{-2} - 0.0496z^{-3} + 0.00673z^{-4}}{1 - 0.164z^{-1} + 0.0278z^{-2} - 0.00166z^{-3} + 0.000152z^{-4}}.$$

To show that the disturbance rejection algorithm is robust to model uncertainties (recall Remark 1), two inaccurate models, $\hat{P}_{d1}^*(z)$ and $\hat{P}_{d2}^*(z)$, are also tested in simulation. The inaccurate models are obtained by adding parameter uncertainties to the true model. Their differences with $\hat{P}_d^*(z)$ in the frequency domain are shown in Fig. 8.

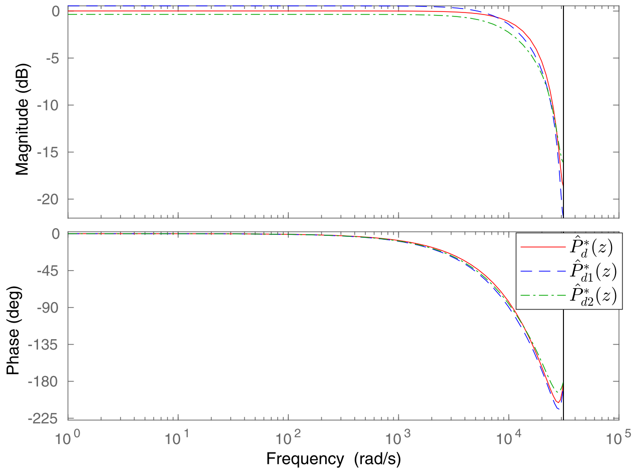

Fig. 8. Bode plot of $\hat{P}_d^*(z)$, $\hat{P}_{d1}^*(z)$ and $\hat{P}_{d2}^*(z)$.

Table 1
Disturbance reduction percentage under different noise levels and with different identified baseline models.

Noise level	$\hat{P}_d^*(z)$	$\hat{P}_{d1}^*(z)$	$\hat{P}_{d2}^*(z)$
0%	99.80	99.88	99.45
7%	99.44	99.25	99.43
14%	98.72	98.62	98.85
28%	96.89	96.60	97.70

We first build the control scheme in Fig. 4 in MATLAB. The minimum sampling time of the vision sensor is limited to 0.3ms. For narrow-band disturbances, one can use the regular disturbance observer [36] to achieve perfect disturbance rejection. However, if the disturbance has frequency components greater than $f_N = 1667$ Hz (the Nyquist frequency of the vision sensor), the actual plant output will be significantly amplified [26]. In simulation, the disturbance d has three frequency components at $0.8f_N$, $1.6f_N$ and $2.3f_N$, respectively. The fast and slow sampling rates are $f_{sf} = 10$ kHz and $f_{ss} = 10/3$ kHz, respectively. Following the example procedure in Section 4, we obtain parameter $\boldsymbol{b}$ in (21):

$$\boldsymbol{b} = \begin{bmatrix} -0.1668 & 0.7440 & 0.7068 & 0.6715 & -0.1359 & 0.7351 \end{bmatrix}^T.$$

and parameters $\boldsymbol{w}_1$ and $\boldsymbol{w}_2$:

$$\boldsymbol{w}_1 = \begin{bmatrix} -0.0365 & -0.0877 & 0.1119 & -0.1501 & -0.0110 & 0.1043 \end{bmatrix}^T,$$

$$\boldsymbol{w}_2 = \begin{bmatrix} -0.0688 & -0.0045 & 0.1522 & -0.1023 & 0.0903 & -0.0051 \end{bmatrix}^T.$$

Fig. 9 shows the system output sampled at 10 kHz. The dotted and solid lines are the system outputs when the proposed compensation scheme is turned off and on, respectively. The results indicate that the proposed algorithm has the ability of full disturbance rejection, as the fast-sampled outputs converge to zero when the proposed algorithm is turned on. We also tested the control scheme under different noise levels and model uncertainties. Disturbance reduction performance is compared by measuring the reduction percentage of the highest system output amplitude at steady state. The test results are shown in Table 1. Here, the noise is a uniformly distributed random signal, and the noise level is the ratio between the maximum noise amplitude and the maximum disturbance amplitude. The test results show that the disturbance reduction performance remains high even when the noise level is increased from 0 to 28% and the proposed algorithm is highly robust to model uncertainty.

Fig. 10 shows the time-domain disturbance reconstruction results by the IIR predictor. The dotted line represents the real-time disturbance signal. The slowly measured disturbance samples are marked with cross

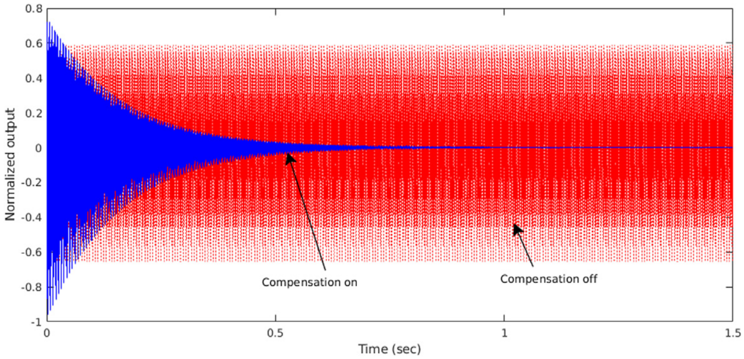

Fig. 9. System output sampled at 10 kHz.

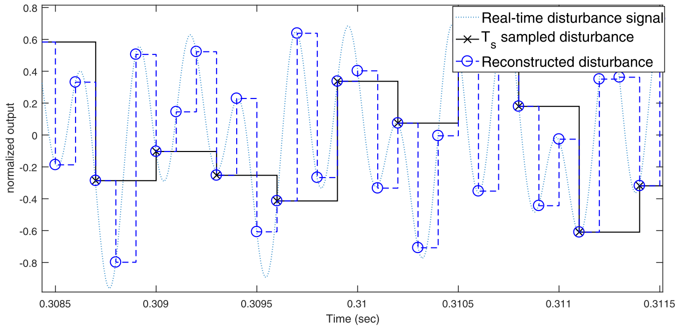

Fig. 10. Disturbance reconstruction results by IIR predictor with $\alpha = 0.95$.

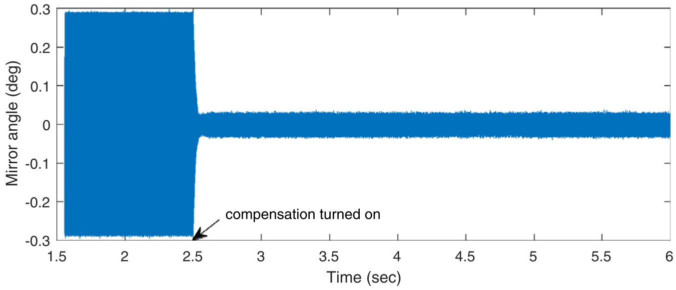

Fig. 11. Galvo scanner outputs sampled at 10 kHz.

marks, and the reconstructed disturbance samples are marked with circle marks. In the simulation, we added a white noise with a noise level of 4% to the input of IIR predictor. The predictor successfully recovered the intersample data from the noisy and slow-sampled signal.

In the experiment on the galvo scanner testbed, we feed a 2000 Hz beyond-Nyquist disturbance into the system. Fig. 11 shows the sampled time-domain system outputs sampled at 10 kHz. After the disturbance compensation loop is enabled at $t = 2.5$ s, the outputs drop dramatically, yielding a 90% reduction of the regulation errors (Compared to the simulation results, there was measurement noise in the scanner outputs). The disturbance rejection result is also observed in the frequency domain (Fig. 12). When the compensation loop is disabled, the outputs have a large spike at 2000 Hz, which disappears after turning on the proposed algorithm.

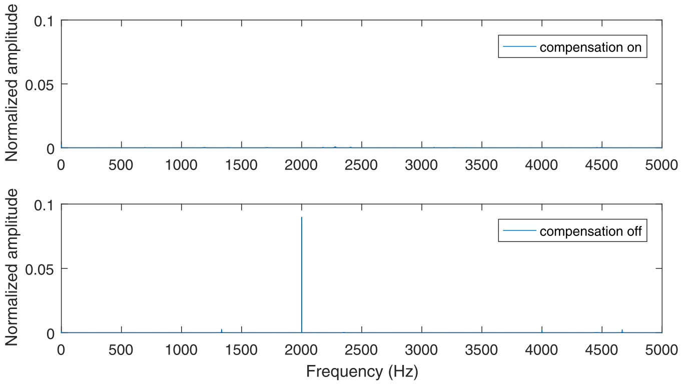

Fig. 12. FFT of the galvo scanner outputs sampled at 10 kHz.

6. Conclusion

In this paper, the problem of beyond-Nyquist disturbance rejection is addressed with application to beam steering in selective laser sintering. Based on frequency information about the disturbance, we designed a multi-rate model-based predictor that can accurately recover the intersample disturbance information from slowly sampled measurements. Combined with a forward model disturbance estimation structure, the proposed algorithm enables the possibility of fully rejecting beyond Nyquist narrow-band disturbances. Both the simulated and experimental results show the effectiveness of the proposed algorithm.

Other than the focused SLS process, the proposed control scheme is expected to apply to systems where beyond-Nyquist disturbances exist, and the sensor sampling rate is limited. Future work includes the extension to other disturbance structures (e.g., general periodic signals and signal with a moving-average model, etc.) and other application domains.

Acknowledgments

This work was partially sponsored by the United Technologies Corporation Institute for Advanced Systems Engineering (UTC-IASE) of the University of Connecticut and an NSF CMMI Award 1750027. Any opinions expressed herein are those of the authors and do not represent those of the sponsor.

References

[1] Lott P, Schleifenbaum H, Meiners W, Wissenbach K, Hinke C, Bültmann J. Design of an optical system for the in situ process monitoring of selective laser melting (SLM). Phys Procedia 2011;12:683–90.
[2] Gibson I, Rosen DW, Stucker B, et al. Additive manufacturing technologies, 238. Springer; 2010.
[3] Wang D, Chen X. A multirate fractional-order repetitive control for laser-based additive manufacturing. Control Eng Pract 2018;77:41–51.
[4] Orzechowski PK, Chen NY, Gibson JS, Tsao T-C. Optimal suppression of laser beam jitter by high-order RLS adaptive control. IEEE Trans Control Syst Technol 2008;16(2):255–67.
[5] Orzechowski PK, Gibson S, Tsao T-C, Herrick D, Mahajan M, Wen B. Adaptive suppression of optical jitter with a new liquid crystal beam steering device. Defense and security symposium. International Society for Optics and Photonics; 2007. 65690V–65690V.
[6] Perez-Arancibia NO, Gibson JS, Tsao T-C. Frequency-weighted minimum-variance adaptive control of laser beam jitter. IEEE/ASME Trans Mechatron 2009;14(3):337–48.

[7] Mnerie CA, Preitl S, Duma V-F. Performance enhancement of galvanometer scanners using extended control structures. In: Applied computational intelligence and informatics (SACI), 2013 IEEE 8th international symposium on. IEEE; 2013. p. 127–30.

[8] Mnerie C, Preitl S, Duma V-F. Galvanometer-based scanners: mathematical model and alternative control structures for improved dynamics and immunity to disturbances. Int J Struct Stab Dyn 2017:1740006.

[9] Mnerie CA, Preitl S, Duma V-F. Classical PID versus predictive control solutions for a galvanometer-based scanner. In: Applied computational intelligence and informatics (SACI), 2015 IEEE 10th jubilee international symposium on. IEEE; 2015. p. 349–53.

[10] Orzechowski PK, Gibson S, Tsao T-C. Disturbance rejection by optimal feedback control in a laser beam steering system. In: ASME 2004 international mechanical engineering congress and exposition. American Society of Mechanical Engineers; 2004. p. 55–62.

[11] Yoo HW, Ito S, Schitter G. High speed laser scanning microscopy by iterative learning control of a galvanometer scanner. Control Eng Pract 2016;50:12–21.

[12] Yuan P, Gu D. Molten pool behaviour and its physical mechanism during selective laser melting of TiC/AlSi10Mg nanocomposites: simulation and experiments. J Phys D Appl Phys 2015;48(3):035303.

[13] Craeghs T, Clijsters S, Kruth J-P, Bechmann F, Ebert M-C. Detection of process failures in layerwise laser melting with optical process monitoring. Phys Procedia 2012;39:753–9.

[14] Berumen S, Bechmann F, Lindner S, Kruth J-P, Craeghs T. Quality control of laser-and powder bed-based additive manufacturing (AM) technologies. Phys Procedia 2010;5:617–22.

[15] Yadroitsev I, Krakhmalev P, Yadroitsava I. Selective laser melting of Ti6Al4V alloy for biomedical applications: temperature monitoring and microstructural evolution. J Alloys Compd 2014;583:404–9.

[16] Price S, Lydon J, Cooper K, Chou K. Temperature measurements in powder-bed electron beam additive manufacturing. ASME 2014 international mechanical engineering congress and exposition. American Society of Mechanical Engineers; 2014. V02AT02A002–V02AT02A002.

[17] Wegner A, Witt G. Process monitoring in laser sintering using thermal imaging. In: Proc. int. solid free. fabr. symp; 2011.

[18] Chaumette F, Hutchinson S. Visual servo control. I. Basic approaches. IEEE Rob. Autom. Mag. 2006;13(4):82–90.

[19] Drexler W, Liu M, Kumar A, Kamali T, Unterhuber A, Leitgeb RA. Optical coherence tomography today: speed, contrast, and multimodality. J Biomed Opt 2014;19(7):071412.

[20] Duma V-F, Tankam P, Huang J, Won J, Rolland JP. Optimization of galvanometer scanning for optical coherence tomography. Appl Opt 2015;54(17):5495–507.

[21] Sheppard C, Shotton D, Sheppard C. Confocal laser scanning microscopy. Microscopy handbook. New York: BIOS Scientific Publishers Ltd; 1997.

[22] Jerri AJ. The shannon sampling theorem—its various extensions and applications: a tutorial review. Proc IEEE 1977;65(11):1565–96.

[23] Unser M. Sampling-50 years after shannon. Proc IEEE 2000;88(4):569–87.

[24] Yamamoto Y, Nagahara M, Khargonekar PP. Signal reconstruction via H-infinity sampled-data control theory—beyond the shannon paradigm. IEEE Trans Signal Process 2012;60(2):613–25.

[25] Tani J, Mishra S, Wen JT. Motion blur-based state estimation. IEEE Trans Control Syst Technol 2016;24(3):1012–19. doi:10.1109/TCST.2015.2473004.

[26] Chen X, Xiao H. Multirate forward-model disturbance observer for feedback regulation beyond nyquist frequency. Syst Control Lett 2016;94:181–8.

[27] Xiao H, Chen X. Multi-band beyond-nyquist disturbance rejection on a galvanometer scanner system. In: Advanced intelligent mechatronics (AIM), 2017 IEEE international conference on. IEEE; 2017. p. 1700–5.

[28] Li D, Shah SL, Chen T. System identification issues in multirate systems. In: Electrical and computer engineering, 1999 IEEE Canadian conference on, 3. IEEE; 1999. p. 1576–8.

[29] Yan W, Du C, Pang CK. A general multirate approach for direct closed-loop identification to the nyquist frequency and beyond. Automatica 2015;53:164–70.

[30] Pang CK, Yan W, Du C. Multirate identification of mechanical resonances beyond the nyquist frequency in high-performance mechatronic systems. IEEE Trans Syst Man Cybern 2016;46(4):573–81.

[31] Doyle JC, Francis BA, Tannenbaum AR. Feedback control theory. Courier Corporation; 2013.

[32] Regalia PA, Mitra SK, Vaidyanathan P. The digital all-pass filter: a versatile signal processing building block. Proc IEEE 1988;76(1):19–37.

[33] Regalia PA. An improved lattice-based adaptive IIR notch filter. IEEE Trans Signal Process 1991;39(9):2124–8.

[34] Garcia CE, Morari M. Internal model control. a unifying review and some new results. Ind Eng Chem Process Des Dev 1982;21(2):308–23. doi:10.1021/i200017a016.

[35] Ljung L. System identification. Springer; 1998.

[36] Chen X, Tomizuka M. A minimum parameter adaptive approach for rejecting multiple narrow-band disturbances with application to hard disk drives. IEEE Trans Control Syst Technol 2012;20(2):408–15.